



**HAL**  
open science

## **X-ray diffraction setup for breast tissue characterization: Experimental validation on beef phantoms**

Vera Feldman, Caroline Paulus, Joachim Tabary, Olivier Monnet,  
Marie-Claude Gentet, Jean-Louis F Hazemann

### ► **To cite this version:**

Vera Feldman, Caroline Paulus, Joachim Tabary, Olivier Monnet, Marie-Claude Gentet, et al.. X-ray diffraction setup for breast tissue characterization: Experimental validation on beef phantoms. Nuclear Instruments and Methods in Physics Research Section A: Accelerators, Spectrometers, Detectors and Associated Equipment, 2020, 972, pp.164075. 10.1016/j.nima.2020.164075 . hal-03490373

**HAL Id: hal-03490373**

**<https://hal.science/hal-03490373>**

Submitted on 22 Aug 2022

**HAL** is a multi-disciplinary open access archive for the deposit and dissemination of scientific research documents, whether they are published or not. The documents may come from teaching and research institutions in France or abroad, or from public or private research centers.

L'archive ouverte pluridisciplinaire **HAL**, est destinée au dépôt et à la diffusion de documents scientifiques de niveau recherche, publiés ou non, émanant des établissements d'enseignement et de recherche français ou étrangers, des laboratoires publics ou privés.



Distributed under a Creative Commons Attribution - NonCommercial 4.0 International License

# X-ray diffraction setup for breast tissue characterization: experimental validation on beef phantoms

Vera Feldman<sup>a,\*</sup>, Caroline Paulus<sup>a</sup>, Tabary Joachim<sup>a</sup>, Olivier Monnet<sup>a</sup>,  
Marie-Claude Gentet<sup>a</sup>, Jean-Louis Hazemann<sup>b</sup>

<sup>a</sup>*Univ. Grenoble Alpes, CEA, LETI, F-38000 Grenoble, France*

<sup>b</sup>*Univ. Grenoble Alpes, CNRS, Inst. NEEL, F-38042 Grenoble, France*

---

## Abstract

Mammography, ultrasound and magnetic resonance imaging are commonly used to diagnose breast cancer. However these imaging techniques produce a significant number of false positive results and lead to unnecessary biopsies. According to the American Cancer Society, more than 50% of breast biopsies turn out negative. Complementary non invasive diagnostic techniques, such as X-Ray Diffraction (XRD), are explored to reduce this number.

In this paper we describe a novel XRD collimation design dedicated to depth-resolved tissue characterization. Experimental results obtained with phantoms composed of beef adipose and muscle tissues are presented.

*Keywords:* X-ray diffraction (XRD), breast imaging, medical diagnostic imaging

---

## 1. Introduction

Breast cancer is a major public health issue as in 2017 it counted around 59,000 new cases and 12,000 deaths in women in France, according to the French

---

\*Corresponding author

*Email addresses:* [v.b.feldman@gmail.com](mailto:v.b.feldman@gmail.com) (Vera Feldman), [caroline.paulus@cea.fr](mailto:caroline.paulus@cea.fr) (Caroline Paulus), [joachim.tabary@cea.fr](mailto:joachim.tabary@cea.fr) (Tabary Joachim), [olivier.monnet@cea.fr](mailto:olivier.monnet@cea.fr) (Olivier Monnet), [marie-claude.gentet@cea.fr](mailto:marie-claude.gentet@cea.fr) (Marie-Claude Gentet), [jean-louis.hazemann@neel.cnrs.fr](mailto:jean-louis.hazemann@neel.cnrs.fr) (Jean-Louis Hazemann)

*Preprint submitted to Nuclear Instruments and Methods in Physics Research Section A March 12, 2020*

National Cancer Institute [1]. However, early detection eases treatment and in-  
5 creases the chances of a positive outcome. For this reason, regular screenings  
are implemented, so as to detect the pathology as early as possible.

Mammography has been chosen for screening as it is fast (10-15 minutes for  
the whole procedure) and has excellent spatial resolution ( $< 100\mu m$ ). It relies  
on X-rays to produce an image, and its contrast depends on the difference of  
10 attenuation coefficients between healthy and pathological breast tissue: tumors  
and micro-calcifications appear lighter than healthy tissue. However, it has been  
demonstrated that the difference of x-ray attenuation coefficients in healthy and  
pathological tissues is small [2, 3]. This is why in some cases, especially in dense  
breasts, the results of a mammography are uncertain, and other imaging tech-  
15 niques, such as breast ultrasound or magnetic resonance imaging (MRI), are  
required to confirm the diagnosis.

Breast MRI and ultrasound can be very useful to inspect regions already marked  
as suspicious after a mammography. They don't rely on ionizing radiation and  
are non invasive. However, both techniques have their downsides: MRI has a  
20 high false-positive rate [4] and ultrasound is more specific than MRI, but also  
less sensitive [5]. This is why the presence of a malignant tumor is always con-  
firmed by anatomopathological analysis on tissues obtained from biopsies. This  
is the most accurate tool for breast cancer diagnosis but it is invasive, stressful  
for the patient and time-consuming for the medical staff. Furthermore, most  
25 biopsies turn out negative [6].

This is why other imaging techniques that would help reduce the number of  
unnecessary biopsies are considered. One of these techniques is X-Ray Diffrac-  
tion (XRD). The measured spectra  $S_{diff}$  depend on the molecular structure of  
the sample and thus can yield better contrast between healthy and pathological  
30 breast tissue than attenuation-based techniques [7–9]. So it can be used as a  
complementary technique, if required after a mammography.

XRD assesses the diffraction profile as a function of energies  $E$  and angles  $\theta$ .  
To describe both of these variables simultaneously a quantity called *momentum*

*transfer* measured in  $\text{nm}^{-1}$  is used. It is defined as :

$$q = \frac{E}{hc} \sin(\theta/2) \quad (1)$$

35 where  $E$  is the energy in keV,  $hc = 1.24 \text{ keV}\cdot\text{nm}$  is the product of the Planck's constant and of the value of light speed in vacuum and  $\theta$  is the angle between incident and diffracted photon directions. According to Bragg's law, diffraction occurs in crystals only when the following condition is verified :

$$\frac{E}{hc} \sin(\theta/2) = q = \frac{n}{2d} \quad (2)$$

where  $n \in \mathbb{N}$  is the diffraction order ( $n = 1$  in this study). The diffraction profile  
40 in crystals presents discrete sharp peaks. In the case of amorphous materials, such as soft tissues, the diffraction profile presents continuous diffraction patterns, which are also representative of their molecular structure. The diffraction profile expressed as a function of the momentum transfer is called *form factor* and noted hereafter as  $F(q)$ .

45 Depending on the method chosen to cover the desired momentum transfer range (usually around  $[0.5 - 4] \text{ nm}^{-1}$ ), a distinction can be made between two XRD system categories: Angle-Dispersive X-Ray Diffraction (ADXRD) uses a monochromatic X-ray beam and measures a diffraction diagram as a function of angles; in Energy-Dispersive X-Ray Diffraction (EDXRD) the diffraction angle  
50 is fixed and measures are made for different X-ray energies using a conventional source. Breast tissue characterization was achieved with an ADXRD system using synchrotron radiation [10, 11]. However, this type of radiation source is hardly available outside research facilities. By contrast, EDXRD requires only spectrally resolved X-ray detectors, which are much easier to access and operate.  
55 This is why EDXRD is preferred for medical applications.

The correlation between EDXRD results and anatomopathological analysis was demonstrated using PixD geometry to illuminate thin (around 5mm) samples [12, 13]. MacCabe *et al* proposed a secondary collimation with coded apertures and demonstrated its effectiveness *ex vivo* on thin sections of human breast samples  
60 [14–16]. However, with pieces thicker than 1 cm characterization becomes

difficult as contributions at different depths are mixed. Different geometries are explored to provide in-depth resolution especially for potential in vivo applications.

We have worked on X-ray diffraction setups for spatially resolved tissue characterization [17–19], and in this paper we propose a new system geometry which  
65 combines ADXRD and EDXRD, and present an experimental study using a breast-simulating phantoms made of beef tissue.

In section 2, the following points will be presented in order to support this study:

- the experimental setup (2.1);
- 70 • the description of the phantoms (2.2);
- the protocol for experimental data processing and analysis (2.3).

Reconstruction and classification results will be presented in section 3, followed by their discussion and a conclusion on this study in section 4.

## 2. Materials & Methods

### 75 2.1. Experimental setup

The system geometry is represented on figure 1. Attenuation and diffracted spectra were acquired separately.

For diffraction measures the X-ray source with tungsten anode was operated at 160 kV and 4 mA without any filtration. The incident beam were collimated  
80 into a 0.3 mm wide pencil beam with 2 pinholes before passing through the phantom described below. The diffracted spectrum was measured after going through the secondary collimation with a spectral detector called Imadif [20].

The secondary collimator is made of tungsten and has 7 slits. Each slit sees a different  $z$  interval with a specific angle distribution. This collimator was  
85 designed by our team specifically for in-depth imaging [21].

Imadif detector is composed of 24 ( $x$  axis) by 8 ( $y$  axis) pixels on a total surface of 660 mm<sup>2</sup> and has a spectral resolution of 4.25% at 60 keV. We used the sub-pixelation technique in order to virtually split each pixel into 8 virtual pixels

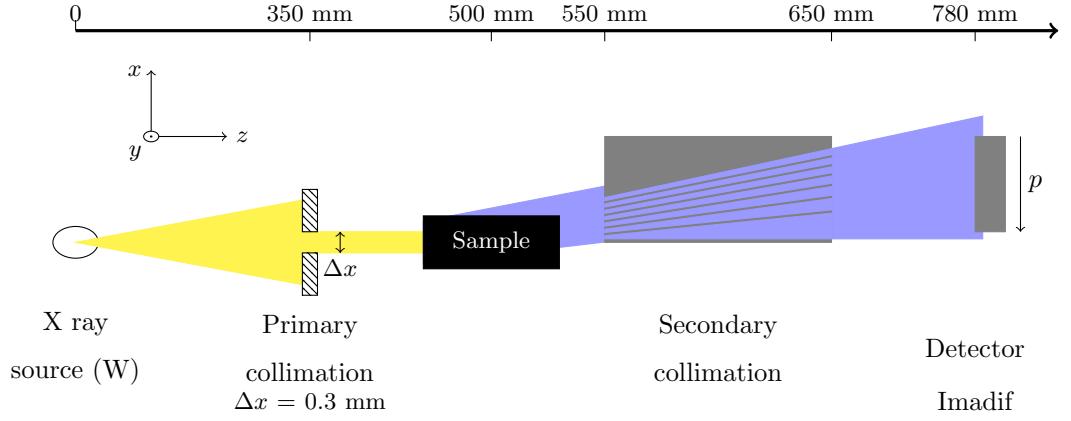


Figure 1: Experimental setup for diffracted spectra acquisition represented in  $(z, x)$  plane. The incident and the diffracted beams are shown respectively in yellow and blue.

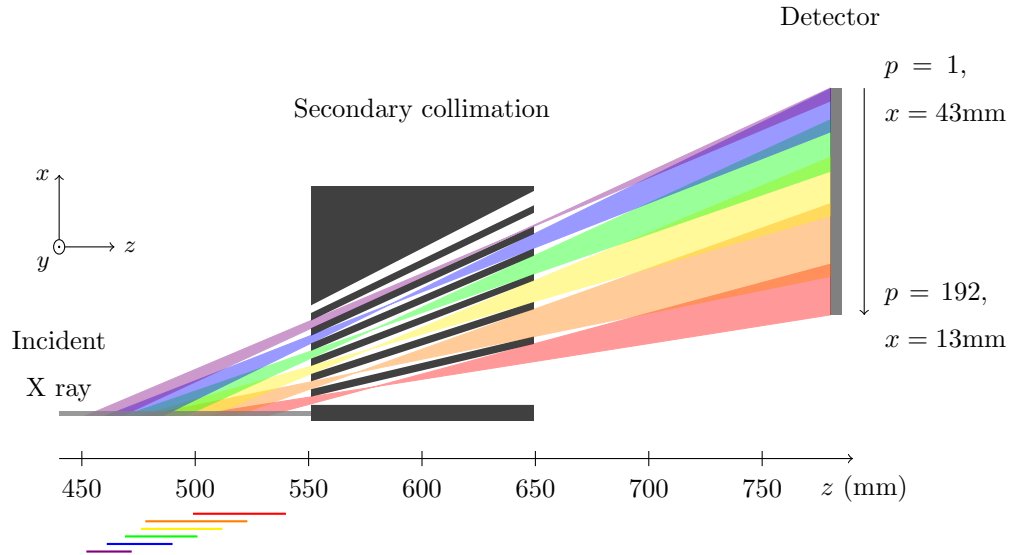


Figure 2: Representation of the field of view of the secondary collimation in the  $(z, x)$  plane. Each color is associated to one slit of the collimator and shows the relation between the positions along the  $z$ -axis and pixels. Below the  $z$  axis, the color bars show the  $z$  intervals seen through each slit. The incident X ray are represented in gray color.

along the  $x$  axis [22]. Thus, a spatial resolution of 192 ( $x$  axis) by 8 ( $y$  axis)  
90 virtual pixels was achieved. For simplicity reasons, virtual pixels are referred to  
as "pixels" hereafter.

## 2.2. Beef tissue phantoms

Five phantoms, shown on the figure 3, were used in this study. They are  
composed of beef adipose tissue (ADP), beef muscle tissue (MSC) and of a mix  
95 of beef adipose and muscle tissue (MIX). The mass proportions used for the  
mix were 65% of beef adipose tissue and 35% of beef muscle tissue. These three  
materials were chosen for the similarity between their diffraction signatures,  
shown on the figure 4a, and breast tissue diffraction signatures, described by  
Pani *et al.*, shown on figure 4b [23]. Breast tissue diffraction signatures, pre-  
100 sented on figure 4b were obtained by energy-dispersive X-ray diffraction com-  
puted tomography. Five types of tissue were studied : adipose, fibrosis, poorly  
and well differentiated cancer and benign breast tissue. Signatures presented on  
figures 4a and 4b are normalized in order to facilitate the comparison between  
curve shapes :

- 105 • the beef adipose tissue (ADP) is used to imitate human adipose tissue;
- the beef muscle tissue (MSC) is used to imitate well differentiated cancer;
- the mix (MIX) is used to imitate fibrosis tissue.

The phantoms ADP-MIX, ADP-MSC and MIX-MSC, shown on figures 3a, 3b  
and 3c, have a triangular geometry. Scanning these phantoms along the  $x$  axis  
110 will provide us with the spatial resolution at the center of the field of view. The  
phantoms MIX-MSC-MIX and MIX-MSC-ADP, shown on figures 3d and 3e,  
present a band of muscle tissue along their diagonal. This band has an almost  
constant width of 10 mm. Scanning these phantoms along the  $x$  axis allows us  
to test whether the muscle tissue can be successfully detected at all  $z$  locations.  
115 For diffraction spectra measurements, the X-ray source was operated at 160 kV  
and 4 mA. Phantoms were scanned along  $x$  axis, for a maximum acquisition

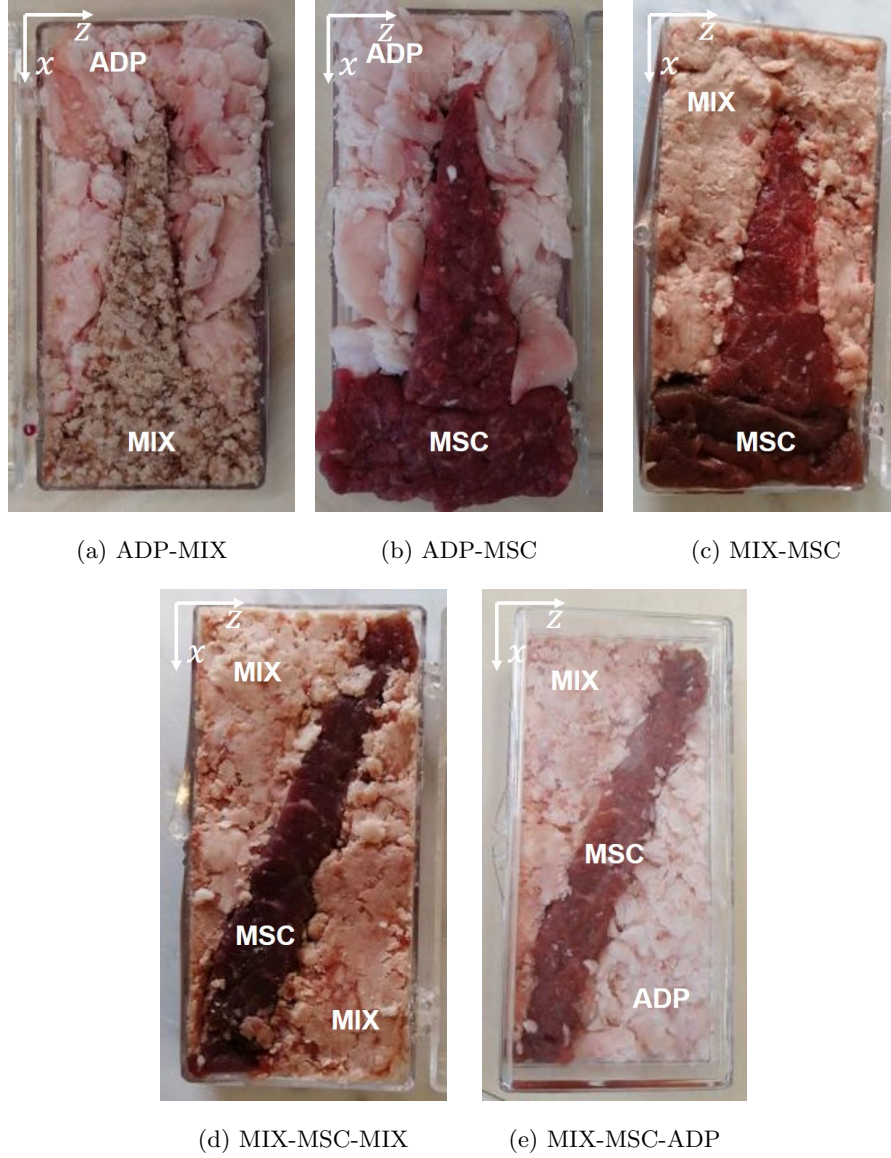


Figure 3: Pictures of five phantoms, made out of adipose tissue (ADP), muscle tissue (MSC) and of a mix of adipose and muscle tissues (MIX): (a) mix and adipose tissue, (b) muscle and adipose tissue, (c) muscle tissue and mix, (d) muscle tissue and mix, (e) adipose tissue, muscle tissue and mix. The containers measure 100 mm by 50 mm by 10 mm ( $z \times x \times y$ ).



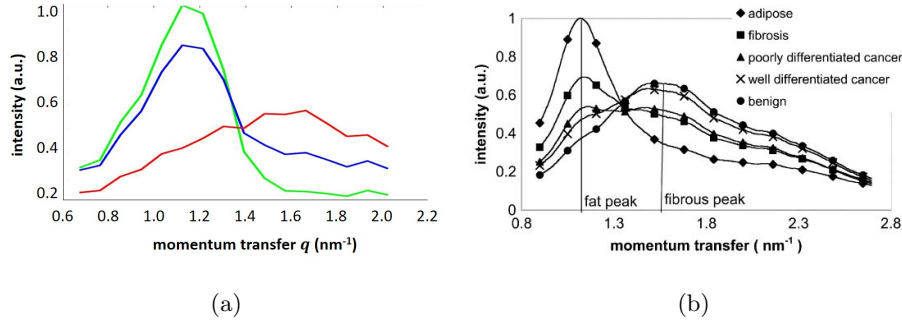


Figure 4: Diffraction signatures : (a) beef adipose tissue (green), beef muscle tissue (red) and mix of beef adipose and muscle tissue (blue), obtained experimentally; (b) different types of breast tissue [23]

time per  $x$  position of 10 seconds. The incremental step in the  $x$ -direction for phantoms ADP-MIX, ADP-MSC, MIX-MSC and MIX-MSC-MIX was 15 mm. The phantom MIX-MSC-ADP was scanned with a smaller incremental step of  
 120 10 mm, as it had the most complex composition, containing all the types of tissue. Diffraction spectra, noted  $S_{diff}(p, E)$ , are measured for each pixel  $p$  and energy channel  $E$ .

Attenuation measures were acquired with the same X-ray source operated at 160 kV and 1 mA without secondary collimation and with MultiX<sup>TM</sup> ME-100  
 125 detector. Attenuation spectra are noted  $S_{att}(E)$ .

### 2.3. Data processing & analysis

The measurements obtained on edge pixels showed significant noise, so we took into account only the measurements from the 4 central columns. Also, among 192 rows of the detector, we used only rows 9 to 184. For each row,  
 130 the variation in diffusion angle  $\theta$  along the 4 columns were considered insignificant (as shown on the figure 5), so diffraction spectra were summed over detector columns ( $y$  axis) as  $y$ -wise resolution is not needed in our experiment. The relation between the in-depth resolved diffraction signature  $F(z, q)$  and the diffracted spectrum  $S_{diff}(p, E)$  is modeled as follows :

$$S_{diff}(p, E) = R(p, E, z, q)F(z, q) \quad (3)$$

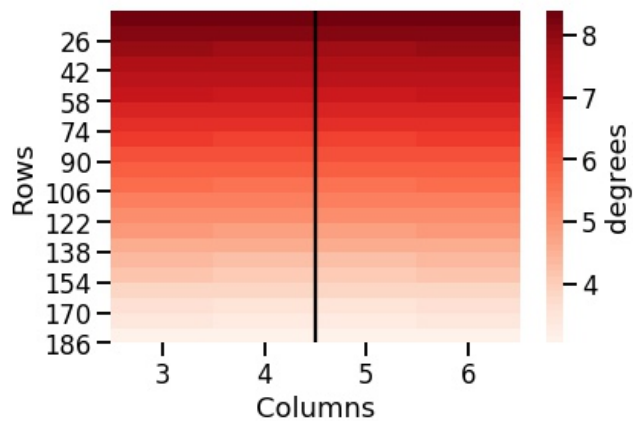


Figure 5: Distribution of  $\theta$  along the selected detector rows and pixels for an object positioned at  $z = 500\text{mm}$ . The color map represents the angle in degrees. The black line shows the middle of the detector along the columns corresponding to  $y = 0$ .

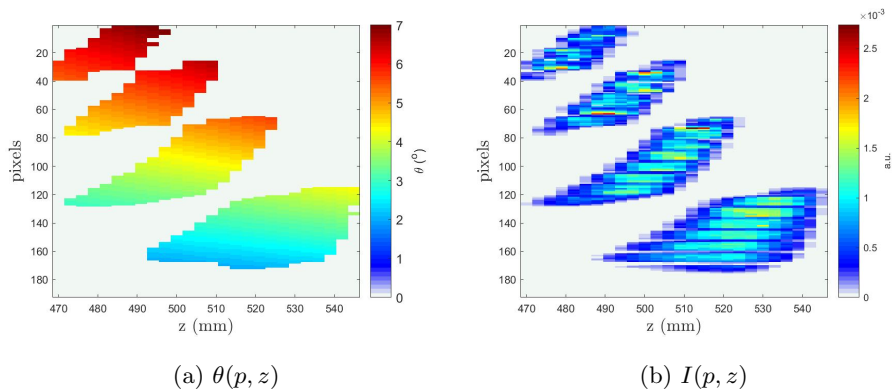


Figure 6: Field of view matrices obtained experimentally through calibration : (a) shows the diffraction angles in degrees and (b) shows the diffraction intensity, relatively to pixels and  $z$  coordinates.

135 where  $R$  is the 4-dimensional forward tensor. It regroups the following elements: detector response matrix, attenuated spectrum (obtained from  $S_{att}(E)$ ) and geometrical response. The construction of this matrix has been detailed in a previous article ([18]). It is similar to a transformation matrix, as it models the changeover from the characterization space  $(z, q)$  to the measure space  $(p, E)$ .

140 The geometrical response is obtained through calibration : a 3 mm-thick aluminum plate is translated along the  $z$  axis by 3 mm steps to cover all the field of view (FOV). The point of this step is to produce a FOV matrix linking detector pixels  $p$  to the position along  $z$  and to the diffraction angle  $\theta$ . We used the aluminum diffraction peak corresponding to  $q = 4.275 \text{ nm}^{-1}$ : for each  $z$

145 position of the calibration plate we note the pixels that "see" this  $z$  position and corresponding energies. From this, we infer a matrix  $M(p, z, \theta)$  representing the ratio between the number of photons seen by the pixel  $p$  coming from a position  $z$  at a diffraction angle  $\theta$ , and the total number of detected photons. This matrix takes into account the system geometry. Figure 6 shows diffraction

150 intensity and angle per  $z$  position and per pixel  $p$ .

The forward matrix  $R(p, E, z, q)$  is obtained by using Bragg's law on the matrix  $M(p, z, \theta)$  and multiplying the corresponding dimensions by the detector response matrix and the attenuated spectrum.

Inverting the model (3) is an ill-posed problem and to obtain an estimation of

155  $F(z, q)$  we used an iterative MLEM algorithm [24].

The calibration step is key to establishing the forward matrix and, as consequence, a correct MLEM inversion.

### 3. Results

As phantoms were scanned along the  $x$  axis, after the reconstruction we

160 obtained diffraction signatures as functions of the  $(x, z)$  position and of the momentum transfer  $q$  :  $F(x, z, q)$ . For visualization purposes, we computed two-dimensional maps  $R_F(x, z)$  for each phantom, defined as :

$$R_F(x, z) = \frac{F_2(x, z)}{F_1(x, z)}$$

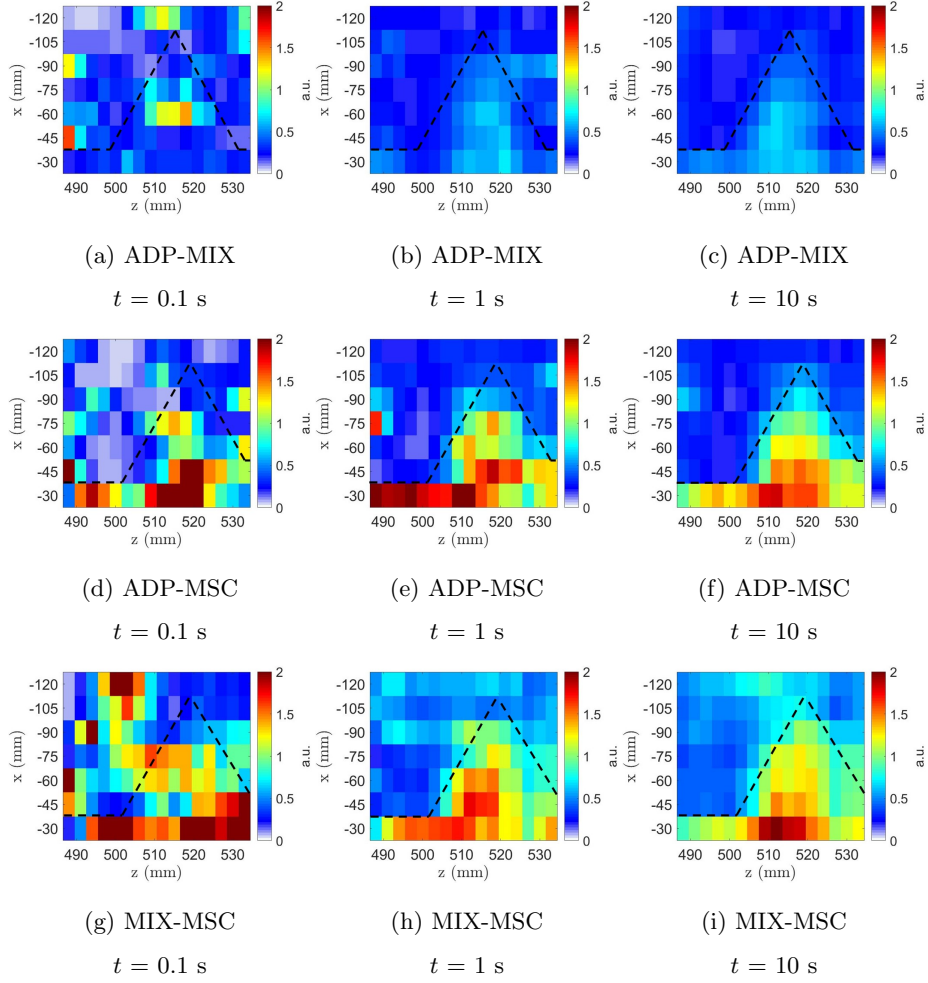


Figure 7:  $R_F$  maps for phantoms ADP-MIX, ADP-MSC and MIX-MSC (row-wise), and different acquisition times (column-wise). The color scale is identical for all figures. "ADP" stands for adipose tissue, "MSC" for muscle tissue, and "MIX" for the mix of adipose and muscle tissue. Dashed black lines are drawn to show the ground truth limits between tissues.

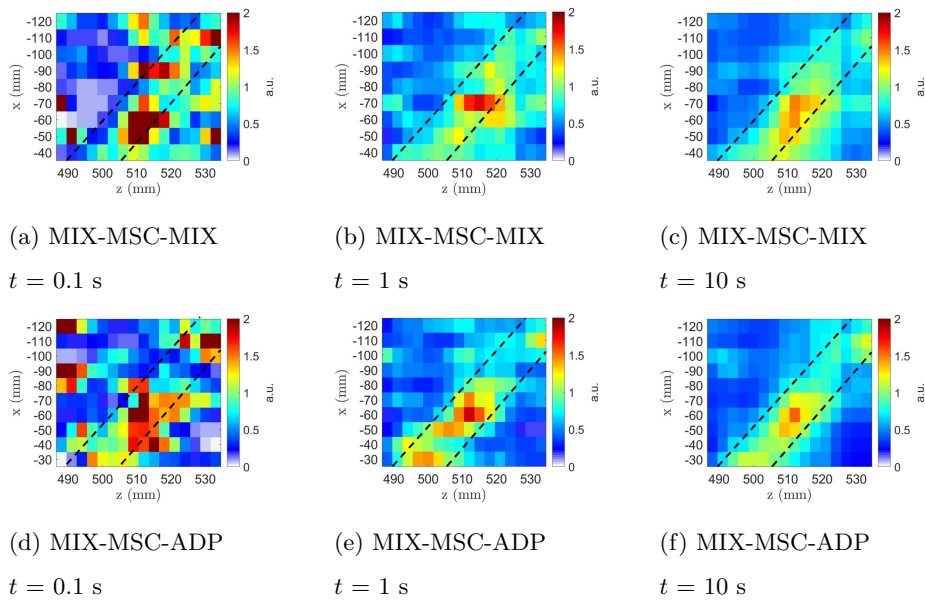


Figure 8:  $R_F$  maps for phantoms MIX-MSC-MIX and MIX-MSC-ADP (row-wise), and different acquisition times (column-wise). The color scale is identical for all figures. "ADP" stands for adipose tissue, "MSC" for muscle tissue, and "MIX" for the mix of adipose and muscle tissue. Dashed black lines are drawn to show the ground truth limits between tissues.

where  $F_1$  and  $F_2$  represent the mean of  $F(x, z, q)$  along the third dimension on the intervals  $Q_1 = [1.0 - 1.2] \text{ nm}^{-1}$  and  $Q_2 = [1.5 - 1.7] \text{ nm}^{-1}$  respectively.   
 165  $Q_1$  corresponds to the interval where the diffraction signatures of adipose tissue and of the mix are maximal, whereas  $Q_2$  corresponds to the interval where the diffraction signature of the muscle tissue is maximal. So, we can expect  $R_F$  to be greater for  $(x, z)$  locations where muscle tissue, imitating well-differentiated breast cancer, is present. On the figures 7 and 8 are shown  $R_F$  maps for all   
 170 phantoms (row-wise) and for acquisition times of 0.1, 1 and 10 seconds (column-wise). The color scale represents the value of  $R_F$  for each  $(x, z)$  position. The span of the color scale is identical for all phantoms and acquisition times. On all figures black or white lines were drawn to materialize the ground truth limits between different tissues.

175 From these maps, we can observe that an acquisition time of 0.1 second is insufficient to recognise the geometry of the phantoms. However, for greater acquisition times the structural patterns of the phantom emerge. As can be seen on figure 7c, the contrast between adipose tissue and the mix is rather small. Whereas the contrast between muscle tissue and adipose tissue, shown   
 180 on figure 7f, or the contrast between muscle tissue and the mix, shown on figure 7i, is greater. Higher values of  $R_F$  follow the expected triangular and diagonal shapes of the muscle tissue. We note on the figures 8c and 8f that muscle tissue is more visible when compared to adipose tissue. This can be expected, as the diffraction signature of the mix is a linear combination of adipose and   
 185 muscle tissues. However, even for phantoms combining muscle tissue and the mix, muscle tissue remains visible on the  $R_F$  maps.

#### 4. Conclusion

This paper presents an experimental setup for energy-resolved measurements   
 190 of diffraction spectra, as well as a data processing method for computing diffraction signatures from these measurements. The system was tested using phan-

toms made of beef adipose and muscle tissues, which were chosen to imitate the diffraction signatures of breast tissues. The phantoms were scanned in order to obtain a two-dimensional characterization.

195 The presented results show that the nature of the tissue (adipose, muscle or a mix of adipose and muscle) can be successfully visualized on  $R_F$  maps for an acquisition time of 10 seconds. This demonstrates the characterization capabilities of our system. Furthermore, as these tissues were chosen to imitate different types of breast tissue, these results give us reason to expect similar results with  
200 human tissue. We hope to test our system on human tissue samples in the near future.

In the end, these results are very encouraging and show the potential of X-ray diffraction for clinical applications in breast cancer diagnosis. To further improve the results, a classification algorithm could be implemented in order  
205 to automatically attribute a label, such as "healthy" or "pathological", to a given location in the sample. Furthermore, the absorbed radiation dose must be carefully studied.

## References

- [1] Institut National du Cancer, Les cancers en France, [www.e-cancer.fr](http://www.e-cancer.fr)  
210 (2017).
- [2] P. C. Johns, M. J. Yaffe, X-ray characterisation of normal and neoplastic breast tissues, *Physics in Medicine & Biology* 32 (6) (1987) 675–695.
- [3] R. Chen, R. Longo, L. Rigon, F. Zanconati, A. De Pellegrin, F. Arfelli, D. Dreossi, R.-H. Menk, E. Vallazza, T. Xiao, E. Castelli, Measurement of  
215 the linear attenuation coefficients of breast tissues by synchrotron radiation computed tomography, *Physics in Medicine & Biology* 55 (17).
- [4] A. Raikhlin, B. Curpen, E. Warner, C. Betel, B. Wright, R. Jong, Breast MRI as an Adjunct to Mammography for Breast Cancer Screening in High-

- Risk Patients: Retrospective Review, American Journal of Roentgenology  
220 204(4) (2015) 889–897.
- [5] H. He, J. Plaxco, W. Wei, L. Huo, R. P. Candelaria, H. M. Kuerer, W. T. Yang, Incremental cancer detection using breast ultrasonography versus breast magnetic resonance imaging in the evaluation of newly diagnosed breast cancer patients, The British Journal of Radiology 89(1065).
- 225 [6] American Cancer Society, Breast biopsy, <https://www.cancer.org/cancer/breast-cancer/screening-tests-and-early-detection/breast-biopsy.html>.
- [7] G. Kidane, R. D. Speller, G. J. Royle, A. M. Hanby, X-ray scatter signatures for normal and neoplastic breast tissues, Physics in Medicine & Biology  
230 44 (7) (1999) 1791–1802.
- [8] E. J. Harris, G. J. Royle, R. D. Speller, J. A. Griffiths, G. Kidane, A. M. Hanby, Evaluation of a novel low light level (13 vision) ccd technology for application to diffraction enhanced breast imaging, Nuclear Instruments and Methods in Physics Research, Section A: Accelerators, Spectrometers, and Detectors and Associated Equipment 513 (2003) 27–31.  
235
- [9] C. C. E. Crews, D. O’Flynn, A. Sidebottom, R. D. Speller, Quantitative energy-dispersive x-ray diffraction for identification of counterfeit medicines: A preliminary study, in: Proceedings of SPIE, Vol. 9482, 2015.
- 240 [10] M. Fernandez, J. Keyrilinen, R. Serimaa, M. Torkkeli, M.-L. Karjalainen-Lindsberg, M. Tenhunen, W. Thomlinson, V. Urban, P. Suortti, Small-angle x-ray scattering studies of human breast tissue samples, Physics in Medicine & Biology 47 (4) (2002) 577–592.
- 245 [11] M. Fernandez, J. Keyrilinen, M.-L. Karjalainen-Lindsberg, M. Leidenius, K. von Smitten, S. Fiedler, P. Suortti, Human breast tissue characterisation with small-angle x-ray scattering, Spectroscopy 18 (2) (2004) 167–176.



- [12] D. O'Flynn, C. B. Reid, C. Christodoulou, M. D. Wilson, M. C. Veale, P. Seller, D. Hills, H. Desai, B. Wong, R. Speller, Explosive detection using pixellated x-ray diffraction (pixd), *Journal of Instrumentation* 8 (3).
- [13] R. M. Moss, A. S. Amin, C. Crews, C. A. Purdie, L. B. Jordan, F. Iacoviello, A. Evans, R. D. Speller, S. J. Vinnicombe, Correlation of x-ray diffraction signatures of breast tissue and their histopathological classification, *Scientific Reports* 7 (1).
- [14] K. MacCabe, K. Krishnamurthy, A. Chawla, D. Marks, E. Samei, D. Brady, Pencil beam coded aperture x-ray scatter imaging, *Optics Express* 20 (15) (2012) 16310–16320.
- [15] M. N. Lakshmanan, J. A. Greenberg, E. Samei, A. J. Kapadia, Experimental implementation of coded aperture coherent scatter spectral imaging of cancerous and healthy breast tissue samples, in: *Proceedings of SPIE*, Vol. 9412, 2015.
- [16] J. R. Spencer, J. E. Carter, C. K. Leung, S. J. McCall, J. A. Greenberg, A. J. Kapadia, Coded aperture coherent scatter spectral imaging for assessment of breast cancers: an ex-vivo demonstration, in: *Proceedings of SPIE*, Vol. 10132, 2017.
- [17] F. Marticke, G. Montémont, C. Paulus, O. Michel, J. I. Mars, L. Verger, Simulation study of an x-ray diffraction system for breast tumor detection, *Nuclear Instruments and Methods in Physics Research, Section A: Accelerators, Spectrometers, Detectors and Associated Equipment* 867 (2017) 20–31.
- [18] D. Barbes, J. Tabary, C. Paulus, J.-L. Hazemann, L. Verger, Material-specific imaging system using energy-dispersive x-ray diffraction and spatially resolved cdznte detectors with potential application in breast imaging, *Nuclear Instruments and Methods in Physics Research A* 848 (2017) 91–98.

- [19] V. Feldman, J. Tabary, C. Paulus, J.-L. Hazemann, O. Filhol, I. Vilgrain, L. Verger, Ex-vivo mice mammary glands characterization using energy-dispersive x-ray diffraction and spacially resolved CdZnTe detectors, in: Proceedings of SPIE, Vol. 10573, 2018.
- 275
- [20] G. Montémont, D. Kosciesza, O. Monnet, S. Stanchina, J. P. Schlomka, L. Verger, An autonomous czts module for x-ray diffraction imaging, in: 2013 IEEE Nuclear Science Symposium and Medical Imaging Conference (2013 NSS/MIC), 2013.
- 280
- [21] D. Barbes, Nouveaux systèmes d'imagerie médicale exploitant la diffraction x en dispersion d'énergie à l'aide de détecteurs spectrométriques CdZnTe, Ph.D. thesis, Université Grenoble Alpes (2016).
- [22] J. Tabary, C. Paulus, G. Montémont, L. Verger, Impact of sub-pixelation within cdznte detectors for x-ray diffraction imaging systems, in: Proceedings of SPIE, Vol. 10187, 2017.
- 285
- [23] S. Pani, E. J. Cook, J. A. Horrocks, J. L. Jones, R. D. Speller, Characterization of breast tissue using energy-dispersive x-ray diffraction computed tomography, Applied Radiation and Isotopes 68 (10) (2010) 1980–1987.
- [24] L. Shepp, Y. Vardi, Maximum likelihood reconstruction for emission tomography, IEEE Transactions on Medical Imaging 1 (2) (1982) 113–122.
- 290